Banner appropriate to article type will appear here in typeset article

# Constraints on the depth of gas giants' polar vortices from gravito-inertial instability

- Yilin Wang<sup>1</sup>, Tao Cai<sup>2</sup>† and Jun Yang<sup>3</sup>
- <sup>1</sup>School of Physics, Peking University, Beijing, P.R. China
- <sup>2</sup>State Key Laboratory of Lunar and Planetary Sciences, Macau University of Science and Technology, 5
- Macau, P.R. China
- 7 <sup>3</sup>Department of Atmospheric and Oceanic Sciences, Peking University, Beijing, P.R. China
- (Received xx; revised xx; accepted xx)

#### 1. Introduction 9

Jupiter and Saturn are gas giants in our solar system, both featuring prominent polar vortices.

At Jupiter's poles, cyclones form striking geometric arrangements: an octagon in the north

and a pentagon in the south (Adriani et al. 2018, 2020; Tabataba-Vakili et al. 2020), often 12

referred to as 'vortex crystals' (Fine et al. 1995; Siegelman et al. 2022). Each cyclone within 13

these formations spans thousands of kilometers, and the associated shear wind speeds can 14

reach about  $100ms^{-1}$  (Grassi et al. 2018). These cyclones rotate with periods of approximately 15

1–3 days(Adriani et al. 2018), which corresponds to the inertial timescale. In comparison, 16

Jupiter's planetary rotation period is about 10 hours, making the rotational timescale several 17

times shorter than the inertial timescale and highlighting the dominant role of rotational 18

effects. At Saturn's poles, a massive polar cyclone dominates each region, extending from 19

the pole to about 75° latitude. The maximum wind speed within these vortices can reach 20 about 100ms<sup>-1</sup> (Godfrey 1988; Sánchez-Lavega et al. 1993) at the north pole and up to

21

160ms<sup>-1</sup> (Sánchez-Lavega et al. 2006) at the south pole. Similar to Jupiter's polar vortices, 22

Saturn's polar vortices are also strongly influenced by rotational effects. 23

### 2. The model

In the polar regions of a rotating planet, the dynamics of an incompressible Boussinesq fluid 25

can be described using the gamma-plane approximation. This framework accounts for the 26

variation of the Coriolis parameter with radial distance from the pole. The dimensionless 27

governing equations for mass, momentum, and energy conservation in an inviscid stably 28

stratified flow are expressed as follows 29

$$\nabla \cdot \boldsymbol{u} = 0 \,, \tag{2.1}$$

31 
$$\partial_t \boldsymbol{u} = -\boldsymbol{u} \cdot \nabla \boldsymbol{u} - \nabla p - \operatorname{Ro}^{-1} \Gamma^{-1} \left( 1 - \gamma r_0^2 \right) \hat{\boldsymbol{z}} \times \boldsymbol{u} + \operatorname{Fr}^{-2} \theta \hat{\boldsymbol{z}} , \qquad (2.2)$$

$$\partial_t \theta = -\mathbf{u} \cdot \nabla \theta - \mathbf{u} \cdot \hat{\mathbf{z}} \,, \tag{2.3}$$

† Email address for correspondence: tcai@must.edu.mo

where u denotes the velocity field, p is the modified pressure (pressure divided by the reference density), and  $\theta$  represents the perturbation from the background temperature profile.  $\hat{z}$  is a unit vector in the vertical direction. The parameter  $\gamma$  captures the spatial variation of the Coriolis parameter in the vicinity of the pole, while  $r_0$  is the radial distance from the pole. The characteristic vertical and horizontal length scales are denoted by H and R, respectively, and their ratio defines the aspect ratio  $\Gamma = R/H$ . To characterize the dynamical regime of the flow, we introduce two nondimensional parameters. The Rossby number, Ro =  $V/2\Omega_0 R$ , quantifies the relative importance of inertial forces compared to the Coriolis effect, where V is a characteristic velocity and  $\Omega_0$  is the planetary rotation rate. The Froude number, Fr = V/NH, quantifies the ratio of inertial to buoyancy forces in a stratified flow. The Brunt-Väsälä frequency N is defined as  $N = \sqrt{-\rho_0^{-1}gd\rho_0/dz}$ , where  $\rho_0$  is the background density and g is the gravitational acceleration, respectively. It should be noted that different characteristic length scales are used in defining the Rossby and Froude numbers. Specifically, the Rossby number is based on the horizontal length scale R, reflecting the influence of planetary rotation on horizontal motions. In contrast, the Froude number uses the vertical length scale H, capturing the balance between inertial and buoyancy forces in the stratified vertical structure of the flow. The Coriolis effect is incorporated using the  $\gamma$ -plane approximation. Similar to the more widely used  $\beta$ -plane model, this approach expands the Coriolis parameter  $f = 2\Omega_0 \cos \theta$  around the pole, where  $\theta$  is the colatitude, and retains terms up to the second order. While the  $\beta$ -plane approximation assumes a linear variation of the Coriolis parameter with latitude, making it suitable for mid to low latitudes, the gamma-plane approximation is tailored for polar regions. In these areas, the Coriolis parameter varies quadratically with latitude, expressed as  $f = 2\Omega_0(1 - \gamma r_0^2)$ , providing a more accurate representation of rotational effects near the poles. 

We examine a barotropic vortex within a Boussinesq flow. In our model, the vortex's maximum velocity V is taken as the characteristic velocity. The radius at which this maximum occurs defines the characteristic horizontal length scale R, while the vortex height represents the vertical length scale H. This choice leads to a nondimensional representation of the vortex, characterized by a circular shear flow  $u_s = (0, r\Omega(r), 0)$ , where  $\Omega(r)$  describes the angular velocity as a function of radial distance r from the vortex center. The angular velocity profile is given by:

$$\Omega(r) = \frac{1}{\Gamma} \exp\left\{ \frac{1}{b} \left[ 1 - \left( \frac{r}{\Gamma} \right)^b \right] \right\}$$
 (2.4)

where b is a shape parameter that controls the sharpness of the velocity gradient. This formulation yields a smooth, axisymmetric flow with a peak velocity at  $r = \Gamma$ , a structure commonly used to represent geophysical vortices. Initially, the vortex is positioned at the pole.

In Boussinesq flow, Schubert & Hack (1982) identified two types of stability relevant to rotating vortices: static stability ( $N^2 > 0$ ) and inertial stability ( $r^{-3}\partial_r m^2 > 0$ ), where  $m = \Omega r^2 + f r^2/2$  represents the total angular momentum. The Froude number quantifies static stability, while the Rossby number characterizes inertial stability. A smaller Fr indicates stronger resistance to vertical displacement, implying greater static stability. For cyclonic vortices, inertial stability in a barotropic setting requires that the radial derivative of angular momentum be positive, i.e.,  $\partial_r m > 0$ . This condition leads to the following expression

$$\Phi(r) = 1 + \text{Ro}\left[2 - \left(\frac{r}{\Gamma}\right)^b\right]\Omega(r) > 0, \qquad (2.5)$$

where  $\Phi(r)$  serves as a diagnostic function for inertial stability. This formulation provides

a quantitative criterion for assessing inertial stability, ensuring that angular momentum increases with radius, a necessary condition for maintaining stability in cyclonic flows. The minimum value of  $\Phi(r)$  occurs at  $r_{\min} = (2+b)^{1/b}$ , with the corresponding minimum given by  $\Phi_{\min} = 1 - b \exp(-1 - b^{-1})$ Ro. For  $\Phi_{\min}$  to remain positive, indicating inertial stability, the Rossby number must satisfy Ro < Ro<sub>c</sub> =  $b^{-1} \exp(1 + b^{-1})$ . If Ro exceeds this critical threshold Ro<sub>c</sub>, the vortex becomes susceptible to inertial instability.

To evaluate the stability of this configuration, we perform both numerical simulations and linear stability analyses. These approaches allow us to track the evolution of perturbations over time and under varying flow conditions, providing insight into the dynamics and resilience of the vortex structure.

### 3. The result

### 3.1. Numerical simulation

For the numerical simulations, we model vortex motion within a  $\gamma$ -plane domain of size  $40 \times 40 \times 1$  using a grid resolution of  $256 \times 256 \times 21$ . In the vertical direction, the dynamic boundaries are treated as impenetrable and stress-free, while the thermal boundaries maintain a fixed temperature. Horizontally, we apply periodic boundary conditions to ensure continuity across the domain. To prevent artificial meridional flow across the domain boundaries, a sponge layer is implemented outside the inscribed circle of the computational box. This layer gradually dampens the velocity field, ensuring that the flow decays rapidly beyond the circle and mimics the effect of a solid boundary in the meridional direction. To solve the hydrodynamic equations, we use a hybrid finite-difference and spectral methods as described in Cai (2021). To reduce the number of prognostic variables, the velocity field is decomposed into toroidal and poloidal components. The horizontal dimensions are treated using Fourier transforms, enabling efficient computation in spectral space. For the vertical direction, a second-order semi-implicit finite-difference scheme is applied to accurately capture vertical variations while ensuring numerical stability.

To begin our analysis, we fix the parameter  $\gamma = 0$  and set the aspect ratio  $\Gamma = 1$ . We then explore the parameter space defined by the Froude number (Fr) ranging from 10<sup>-4</sup> to  $10^3$  and the Rossby number (Ro) from  $10^{-3}$  to  $10^3$ , as illustrated in Fig. 1. Each block in the figure represents the outcome of a single simulation. This parameter space can be categorized into three primary regimes based on the observed dynamical behavior. Regime I (green) corresponds to cases where either the Rossby number (Ro) or the Froude number (Fr) is small, but not necessarily comparable. This regime is characterized by stable dynamics, and simulations typically run without encountering numerical instability. Regime II (red) is characterized by high values of both Ro and Fr. This region is highly unstable, with simulations frequently failing within the first few time steps. Regime III (light and dark blue) occupies the intermediate range, where Ro and Fr are both low and of similar magnitude. This regime is of particular interest, as it consistently displays the vertical vortex splitting behavior. Since the instability in this regime is driven by the combined effects of stratification and rotation, we refer to it as gravito-inertial instability. In addition to these three main regions, a transitional zone (yellow) separates the stable and unstable regimes. This area shows mixed behavior, indicating a gradual shift in system dynamics.

Figure 2 illustrates the evolution of a case in Regime III. In this regime, although both static and inertial stability conditions are satisfied, instability can still develop. The vortex initially tilts and subsequently breaks in the middle. As time progresses, the structure evolves into two distinct vortices, with one residing in the upper layer and the other in the lower layer.

125

126 127 128

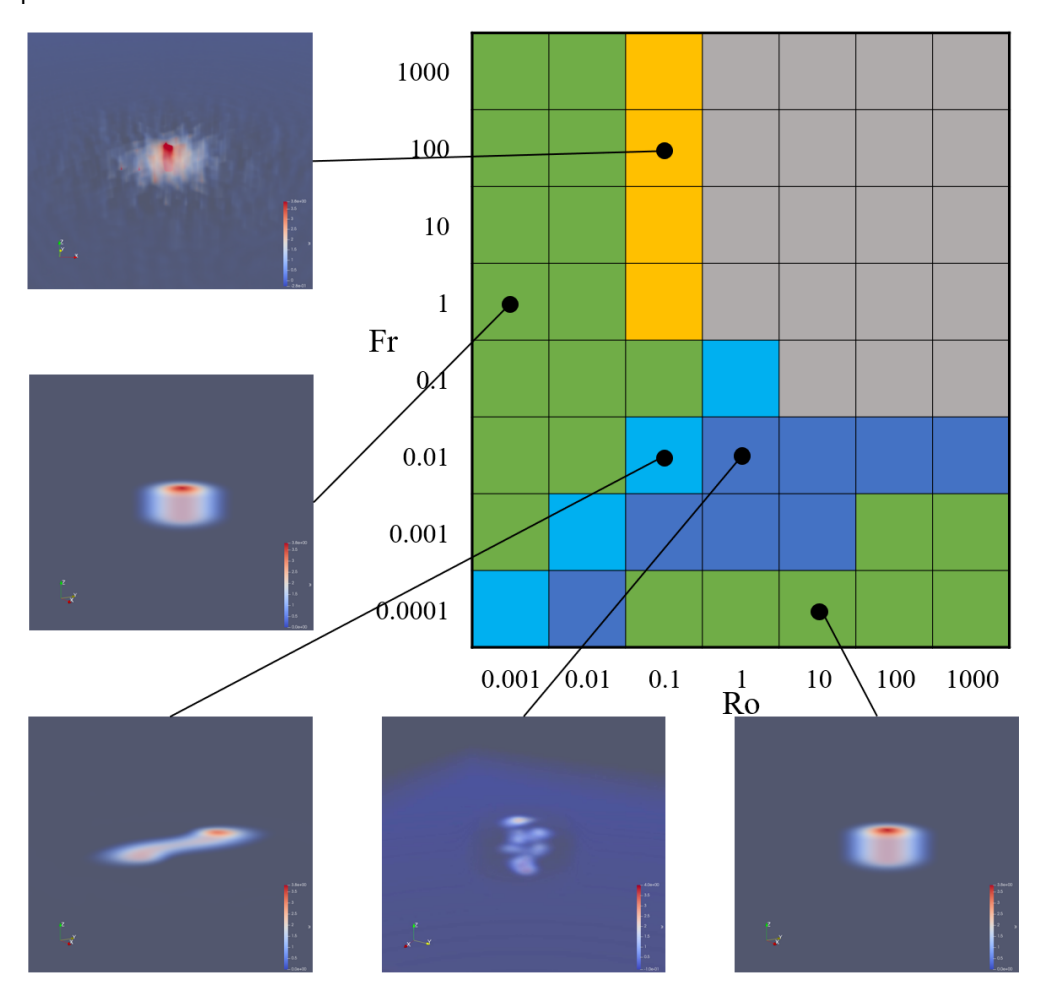


Figure 1: Regimes on flow patterns of vortices across Rossby and Froude number with fixed parameters  $\gamma=0$  and  $\Gamma=1$ .

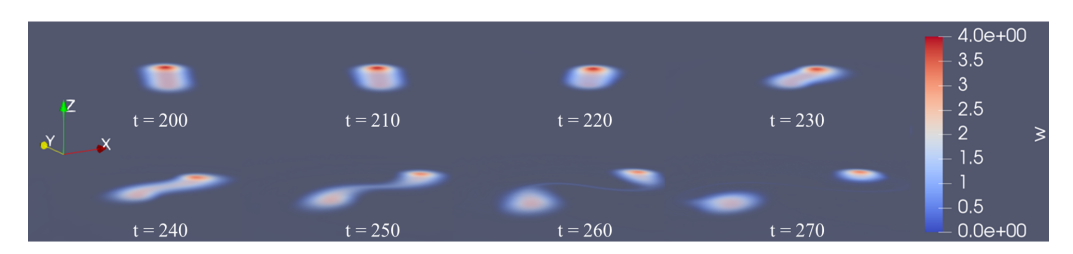


Figure 2: Illustration of vortex splitting for a case in Regime III. Each panel presents a snapshot of the three-dimensional vorticity structure at a given moment as the vortex evolves.

The number of vortex fragments is typically two when  $Fr \approx 0.1$ Ro (the light blue in Fig. 1), but can exceed two when Fr is smaller than 0.1Ro (the dark blue in Fig. 1).

To assess the effect of  $\gamma$  on vortex stability, we performed simulations at Ro = 1 and Fr =  $10^{-3}$  using four values of  $\gamma \in \{0, 1, 2, 4\} \times 10^{-4}$ . In the reference case  $\gamma = 0$ , the vortex split into multiple vortices at t = 2600. For  $\gamma \in 1, 2 \times 10^{-4}$ , splitting still occurred but was

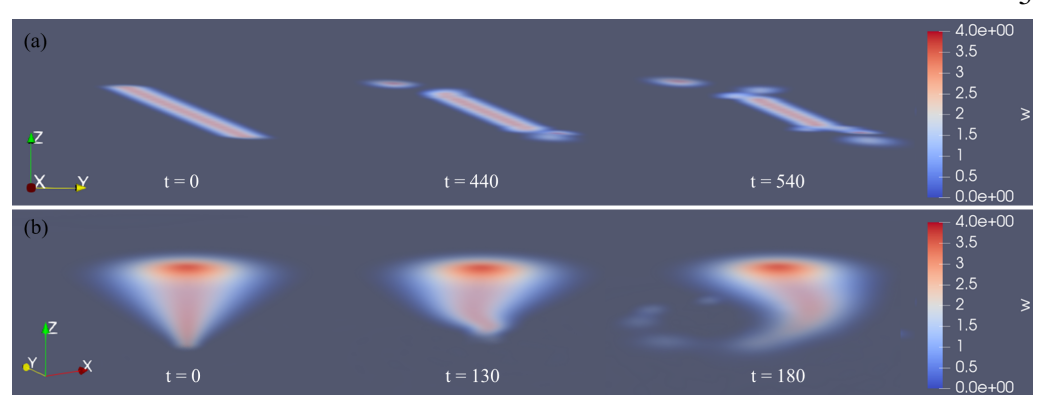


Figure 3

delayed to t=2910 and t=3940, respectively. At  $\gamma=4\times10^{-4}$ , the vortex remained stable for an extended period. These results suggest that increasing  $\gamma$  generally promotes stability. To explore whether this trend persists at larger  $\gamma$ , we performed eight additional simulations at Ro = 0.1 and Fr = 0.01 with  $\gamma$  ranging from  $5\times10^{-5}$  to 0.03. As  $\gamma$  increased from  $5\times10^{-5}$  to  $3\times10^{-4}$ , vortex splitting was progressively delayed. As the  $\gamma$  further increases from 0.001 to 0.01, the vortex remained stable. However, at  $\gamma=0.03$ , the vortex became unstable. This instability arises because a strong  $\gamma$  effect generates a pair of  $\beta$ -gyres within the vortex. When these gyres induce excessive shear, they trigger barotropic instability. In summary,  $\gamma$  has a dual role in vortex stability: weak to moderate values tend to stabilize the vortex, while excessively large values can destabilize it.

We further examine the baroclinic instability of the vortex, considering two configurations: an inclined vortex and a conical vortex. Figure 3(a) shows a simulation with an inclined vortex at Ro = 0.1 and Fr = 0.01. The vortex splits into several smaller vortices, similar to the straight vortex case. Figure 3(b) presents the simulation of a conical vortex Fr = 0.01 by setting the vortex radius linearly increases from the bottom to the top. By this setting, the Rossby number is a function of height, linearly increasing from 1 at the bottom to 0.1 at the top. From Figure 1, we note that at Fr = 0.01, the vortex is stable when Ro = 0.01 but unstable when Ro = 0.1. Consistent with this, Figure 3(b) shows that the bottom layer of the vortex is unstable while the top layer remains stable. Simulations of these two configurations suggest that the observed instability is primarily driven by barotropic effect rather than baroclinic effect.

## 3.2. Linear stability analysis

To investigate the stability of vortex analytically, we perform a linear stability analysis of the system in the cylindrical coordinates  $(r, \phi, z)$  originated at the vortex center. We introduce small perturbations to the initial state, and expanding the resulting equations to first order in the perturbation as

$$\nabla \cdot \boldsymbol{u}' = 0 \,, \qquad (3.1)$$

$$\partial_t \boldsymbol{u}' = -\boldsymbol{u}' \cdot \nabla \boldsymbol{u}_s - \boldsymbol{u}_s \cdot \nabla \boldsymbol{u}' - \nabla \boldsymbol{p}' - \operatorname{Ro}^{-1} \Gamma^{-1} \left( 1 - \gamma r_0^2 \right) \hat{\boldsymbol{z}} \times \boldsymbol{u}' + \operatorname{Fr}^{-2} \theta' \hat{\boldsymbol{z}} , \qquad (3.2)$$

$$\partial_t \theta' = -\boldsymbol{u}_s \cdot \boldsymbol{\nabla} \theta' - \boldsymbol{u}' \cdot \hat{\boldsymbol{z}} , \qquad (3.3)$$

where  $u' = (u'_r, u'_\phi, u'_z)$  is the perturbation of velocity from  $u_s$  in the cylindrical coordinates. All perturbation variables are functions of  $(r, \phi, z, t)$ . We express each variable in normal mode form as  $A'(r, \phi, z, t) \to \tilde{A}(r, z)e^{i(m\phi+\sigma t)}$ , where  $\tilde{A}(r, z)$  is the amplitude, m is the

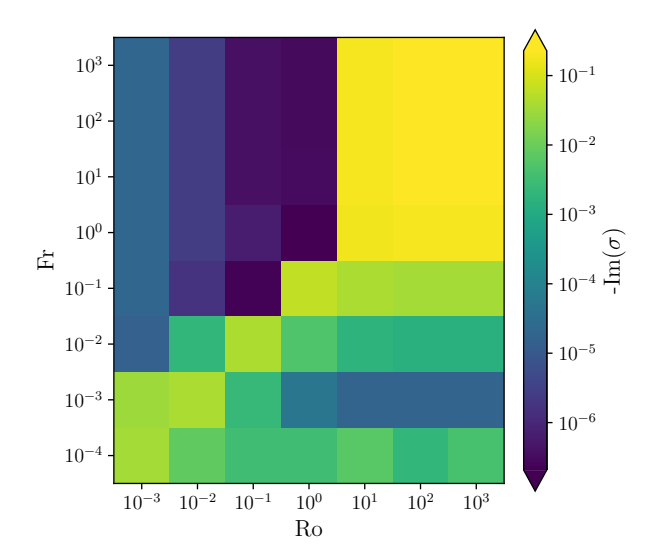


Figure 4: Results from linear stability analysis. Each grid corresponds to the result of a generalized eigenvalue problem with Ro and Fr as indicated in the graph and k = 1, m = 1. The color bar is  $-\text{Im}(\sigma)$ , which means the lower value in the colorbar, the more unstable the corresponding eigenmode is.

azimuthal wavenumber, and  $\sigma$  is the complex frequency. Considering the stress-free boundary condition at the top and bottom boundaries, we can further expand the perturbation variables in the vertical direction as

$$[\tilde{u}_r(r,z), \tilde{u}_{\phi}(r,z), \tilde{p}(r,z)] = \sum_{k=1}^{N} [u_{r,k}(r), u_{\phi,k}(r), p(r)] \cos(k\pi z), \qquad (3.4)$$

$$[\tilde{u}_{z}(r,z),\tilde{\theta}(r,z)] = \sum_{k=1}^{N} [u_{z,k}(r),\theta_{k}(r)] \sin(k\pi z) . \tag{3.5}$$

Substituting the above expansions into the linearized governing equations, and utilizing the orthogonality of the base functions, we obtain a set of generalized eigenvalue problem on  $\sigma$ . The eigenvalue  $\sigma$  determines the growth rate of its corresponding eigenmode. If the imaginary part of  $\sigma$  is negative, then the corresponding eigenmode will grow exponentially with time, leading to instability.

Because the vortex center is singular, the eigenmode can sometimes appear stable at small wavenumbers but unstable at very large wavenumbers. This apparent instability at high wavenumbers is often a numerical artifact. Even if it is physical, perturbations at large k typically decay due to viscous effects. To avoid these complications, we fix the eigenmode at k=1 and m=1 to focus on stability at the smallest wavenumber. The results of the linear stability analysis are shown in Fig. 4. They indicate that the stability pattern is qualitatively consistent with the simulation results. In particular, the vortex becomes unstable when  $Fr \approx 0.1Ro$  and both parameters are small. Based on both the numerical simulations and the linear stability analysis, we conclude that this instability represents a genuine physical phenomenon in vortex dynamics.

### 4. Discussion and Conclusion

181

In this paper, we demonstrate that, in addition to static and inertial instabilities, a distinct 182 gravito-inertial instability emerges when the effects of stratification and rotation are small 183 and comparable. This finding may have important implications for constraining the depth 184 of vortices in planetary atmospheres. For instance, both Jupiter and Saturn host large-scale 185 vortices in their polar regions, with diameters spanning thousands of kilometers. Observations 186 indicate that Jupiter's polar vortices approximately follow a circular shear flow profile with 187 b = 1.5 (Li et al. 2020). The maximum velocity is about 100 m/s achieved at a distance of 188 1000 km from the center of vortex (Grassi et al. 2018). Two scenarios have been proposed 189 for their formation: one suggests that these vortices originate in the shallow weather layer, 190 while the other posits formation within the deep convective zone. If the vortices form in 191 the shallow weather layer, the background atmosphere is convectively stable, which aligns 192 with the idealized conditions considered here in our analysis. The rotation rate of Jupiter 193 is about 10 hours, therefore the Rossby number is about 0.3. In Jupiter's atmosphere, the 194 Brunt-Väsälä frequency N ranges from about  $0.01 \text{ s}^{-1}$  near the 1-bar level (cloud top) to 195  $0.005 \text{ s}^{-1}$  at 10 bars (about 100 km below cloud top) (Simon et al. 2018; Dowling et al. 196 1998, 2006). Below 100 km in depth, N could probably remains less than  $0.005 \text{ s}^{-1}$ . Given 197 that Jupiter's atmosphere extends at most only a few thousand kilometers (Kaspi et al. 2018: 198 Kong et al. 2018; Guillot et al. 2018), the Froude number Fr cannot fall below  $10^{-4}$ . As 199 seen in the Fig. 1, Fr should be on the order of  $Fr \sim 0.1$  for a vortex to remain stable when 200  $Ro \sim 0.1$ . Assuming  $N = 0.005 \text{s}^{-1}$ , this implies a vertical scale height of approximately 201  $H \sim 200$ km. For smaller N, the predicted depth would be even greater, suggesting that 202 Jupiter's large-scale vortices could extend several hundred kilometers below the cloud tops. 203 In Saturn's atmosphere, the polar vortex reaches a peak velocity of about 160 m/s at a 204 radius of roughly 1500 km, corresponding to a Rossby number near 0.3. The Brunt-Väsälä 205 frequency in the cloud region is approximately 0.003 s<sup>-1</sup> (García-Melendo *et al.* 2007; Genio 206 et al. 2009). Applying the same Froude number constraint as before suggests that the depth 207 of these large-scale polar vortices is on the order of 300km at Fr  $\sim 0.1$ . This indicates that 208 209 Saturn's polar vortices also likely could extend several hundred kilometers below the cloud tops. 210

- Funding. This work is partially supported by National Natural Science Foundation of China (No. 12173105),
- the Science and Technology Development Fund, Macau SAR (No. 0147/2023/RIA3), and the Guangdong
- 213 Basic and Applied Basic Research Foundation (No. 2024A1515012239). J.Y. is supported by NSFC funding
- 214 of No. 42275134.
- 215 **Declaration of interests.** The authors report no conflict of interest.
- 216 Author ORCIDs. T. Cai, https://orcid.org/0000-0003-3431-8570; J. Yang, https://orcid.org/0000-0001-
- 217 6031-2485; Y. Wang, https://orcid.org/0009-0006-1862-2424

### REFERENCES

- Adriani, Alberto, Bracco, A, Grassi, Davide, Moriconi, ML, Mura, Alessandro, Orton, G, Altieri, FRANCESCA, Ingersoll, A, Atreya, SK, Lunine, JI & others 2020 Two-year observations of the jupiter polar regions by jiram on board juno. *Journal of Geophysical Research: Planets* 125 (6), e2019JE006098.
- Adriani, Alberto, Mura, Alessandro, Orton, G, Hansen, C, Altieri, Francesca, Moriconi, ML,
   Rogers, J, Eichstädt, G, Momary, T, Ingersoll, Andrew P & others 2018 Clusters of cyclones
   encircling jupiter's poles. *Nature* 555 (7695), 216–219.
- CAI, TAO 2021 Large-scale vortices in rapidly rotating rayleigh-bénard convection at small prandtl number.
   The Astrophysical Journal 923 (2), 138.
- Dowling, TE, Fischer, AS, Gierasch, PJ, Harrington, J, LeBeau Jr, RP & Santori, CM 1998 The explicit planetary isentropic-coordinate (epic) atmospheric model. *Icarus* 132 (2), 221–238.

- Dowling, Timothy E, Bradley, Mary E, Colón, Edward, Kramer, John, LeBeau, Raymond P, Lee,
  Grace CH, Mattox, Timothy I, Morales-Juberías, Raul, Palotai, Csaba J, Parimi, Vimal K
  31 & others 2006 The epic atmospheric model with an isentropic/terrain-following hybrid vertical
  coordinate. *Icarus* 182 (1), 259–273.
- Fine, KS, Cass, AC, Flynn, WG & Driscoll, CF 1995 Relaxation of 2d turbulence to vortex crystals.

  Physical Review Letters **75** (18), 3277.
- 235 GARCÍA-MELENDO, ENRIQUE, SÁNCHEZ-LAVEGA, AGUSTÍN & HUESO, RICARDO 2007 Numerical models of 236 saturn's long-lived anticyclones. *Icarus* 191 (2), 665–677.
- Genio, Anthony D Del, Achterberg, Richard K, Baines, Kevin H, Flasar, F Michael, Read, Peter L,
   Sánchez-Lavega, Agustín & Showman, Adam P 2009 Saturn atmospheric structure and dynamics.
   In Saturn from Cassini-Huygens, pp. 113–159. Springer.
- 240 GODFREY, DA 1988 A hexagonal feature around saturn's north pole. Icarus 76 (2), 335–356.
- GRASSI, DAVIDE, ADRIANI, ALBERTO, MORICONI, ML, MURA, ALESSANDRO, TABATABA-VAKILI, F,
   INGERSOLL, A, ORTON, G, HANSEN, C, ALTIERI, FRANCESCA, FILACCHIONE, GIANRICO & OTHERS
   2018 First estimate of wind fields in the jupiter polar regions from jiram-juno images. *Journal of Geophysical Research: Planets* 123 (6), 1511–1524.
- Guillot, Tristan, Miguel, Y, Militzer, B, Hubbard, WB, Kaspi, Y, Galanti, E, Cao, H, Helled, R,
   Wahl, SM, Iess, L & others 2018 A suppression of differential rotation in jupiter's deep interior.
   Nature 555 (7695), 227–230.
- KASPI, YOHAI, GALANTI, ELI, HUBBARD, WILLIAM B, STEVENSON, DAVID J, BOLTON, SCOTT J, IESS, LUCIANO,
   GUILLOT, TRISTAN, BLOXHAM, JEREMY, CONNERNEY, JACK EP, CAO, HUILI & OTHERS 2018 Jupiter's
   atmospheric jet streams extend thousands of kilometres deep. *Nature* 555 (7695), 223–226.
- Kong, Dali, Zhang, Keke, Schubert, Gerald & Anderson, John D 2018 Origin of jupiter's cloud-level
   zonal winds remains a puzzle even after juno. *Proceedings of the National Academy of Sciences* 115 (34), 8499–8504.
- LI, Cheng, Ingersoll, Andrew P, Klipfel, Alexandra P & Brettle, Harriet 2020 Modeling the stability of polygonal patterns of vortices at the poles of jupiter as revealed by the juno spacecraft. *Proceedings of the National Academy of Sciences* 117 (39), 24082–24087.
- 257 SÁNCHEZ-LAVEGA, A, HUESO, R, PÉREZ-HOYOS, S & ROJAS, JF 2006 A strong vortex in saturn's south pole.
  258 *Icarus* **184** (2), 524–531.
- SÁNCHEZ-LAVEGA, A, LECACHEUX, J, COLAS, F & LAQUES, P 1993 Ground-based observations of saturn's
   north polar spot and hexagon. *Science* 260 (5106), 329–332.
- 261 Schubert, Wayne H. & Hack, James J. 1982 Inertial stability and tropical cyclone development. *Journal* of Atmospheric Sciences **39** (8), 1687 1697.
- SIEGELMAN, LIA, YOUNG, WILLIAM R & INGERSOLL, ANDREW P 2022 Polar vortex crystals: Emergence and structure. *Proceedings of the National Academy of Sciences* **119** (17), e2120486119.
- Simon, Amy A, Hueso, Ricardo, Iñurrigarro, Peio, Sánchez-Lavega, Agustín, Morales-Juberías,
   Raúl, Cosentino, Richard, Fletcher, Leigh N, Wong, Michael H, Hsu, Andrew I, De Pater,
   Imke & others 2018 A new, long-lived, jupiter mesoscale wave observed at visible wavelengths.
   The Astronomical Journal 156 (2), 79.
- Tabataba-Vakili, F, Rogers, JH, Eichstädt, G, Orton, GS, Hansen, CJ, Momary, TW, Sinclair,
   JA, Giles, RS, Caplinger, MA, Ravine, MA & others 2020 Long-term tracking of circumpolar cyclones on jupiter from polar observations with junocam. *Icarus* 335, 113405.